Conductive ZSM-5-Based Adsorbent for CO2 Capture: Active Phase vs Monolith

(Article begins on next page)

27 September 2024

Alessio Masala, Jenny G. Vitillo, Giorgia Mondino, Gianmario Martra, Richard Blom, Carlos A. Grande, Silvia Bordiga

iris-AperTO

1

Conductive ZSM-5-based adsorbent for CO_2

capture: active phase vs. monolith

4 Alessio Masala[†‡], Jenny G. Vitillo[†‡*], Giorgia Mondino[§], Gianmario Martra,[†] Richard Blom,[§]

5 Carlos A. Grande[§] and Silvia Bordiga[†]

6 [†] Department of Chemistry, NIS and INSTM Reference Centre, University of Turin, Via

7 Quarello 15, 10135 Torino, Italy.

8 [§] SINTEF Materials and Chemistry, P.O. Box 124 Blindern, N0314 Oslo, Norway.

9 [‡] The two authors have equally contributed to the manuscript

10

ABSTRACT. Among microporous adsorbents, zeolites constitute the reference materials in CO_2-capture technologies, because of their high CO_2 affinity, high chemical and thermal stability and their low cost. Being synthetized in powder form, they need to be shaped in pellets or monolith before to be suitable for real applications. The process has a direct effect on CO_2-capture properties of the material creating – in this sense – substantial differences between lab-scale (adsorbents) and plant-scale systems (adsorbers). The ability of the honeycomb monolith to efficiently separate gases of interest, arises from the properties of its single components such as an active phase and a phase resulting from the decomposition of a binder. Moreover, the textural (i.e. pore distribution and exposed surface) and structural properties (e.g. amorphization) of the active phase can be modified in the conditions adopted during the process that leads to the final artifact. These modifications can affect the CO_2-capture performances of the active phase. Nevertheless, often a comparison between the active phase and its corresponding monolith is not possible. In this article, the process to obtain a zeolite/electrical conductive carbon monolith suitable for electric swing adsorption (ESA) process is described. The CO_2 adsorption properties of a zeolite (H-ZSM-5) in powder form and its related shaped monolith have been compared to the uptake of other competitive gases (H_2O, O_2 and N_2). The difference in the adsorption properties between the powder and the monolith have been analyzed by means of volumetric, spectroscopic, diffractometric and microscopic techniques. This study underlined the gap between the CO_2-capture performances of pure active phases – usually studied at the lab scale – and their related final artifacts, instead conceived for industrial applications. Interestingly, in the present case, the extrusion of a monolith composed by an active phase and a conductive phase had three positive effects (besides those expected) with respect to the pristine powder: (i)

34   increase in the heat capacity of the material; (ii) decrease the water heat of adsorption; (iii)

35   increase in the CO_2 isosteric heat of adsorption. Whereas the first point is easily correlated to the

36   carbonaceous phase present in the composite, the third can be related to the partial H^+/Na^+

37   exchange occurring along with the monolith preparation, as identified by infrared (IR) and

38   energy dispersive X-Ray spectroscopies (EDS). The increase in the hydrophobicity of the

39   monolith was on the contrary related to both these factors.

40   **1. Introduction**

41   Carbon dioxide capture in post-combustion energy schemes is nowadays considered one of the

42   most viable ways to decarbonize power generation in the short-medium term.[1-4] The advantage

43   of post-combustion CO_2 capture relies on the possibility to retro-fit this technology to already

44   existing power plants.[3] The state-of-the-art for CO_2 capture from post-combustion flue gases is a

45   process based on chemical fixation by aqueous alkanolamine solutions, normally termed as

46   amine scrubbing. This process is however characterized by regeneration-costs issues.[5]

47   Adsorption potentially ensures a weaker bonding between CO_2 and porous solids than the one

48   usually detected for amine-scrubbing process:[6, 7] the energy penalty related to the CO_2-capture

49   process can be minimized when the CO_2 energy of adsorption reaches an optimal value, as

50   demonstrated by Pirngruber, Smit and Sholl.[8-10] Moreover, typical properties of solid adsorbents

51   – zeolites, active carbons or the new generation metal-organic frameworks – such as a low heat

52   capacity (important for temperature swing adsorption, TSA)[3, 11, 12] and a low-medium strength

53   interaction with CO_2,[13-15] offer the possibility to reduce the energetic cost of the recovery step.[6,

54   16]

55 However, the implementation of carbon capture technology on a large scale industrial facility

56 requires a series of engineering features that have to be taken into account when designing the

57 solid adsorbent to be coupled with a CO_2–capture unit. In fact, the use of adsorbents – usually

58 microporous materials with high affinity for CO_2 – in their granular/powder state often implies

59 poor adsorption per unit volume, large pressure drops[17-19] and low thermal conductivity along the

60 fixed-bed length, leading to strong decreases in the uptake capacity (up to 50%).[20] The

61 employment of an adsorbent with the proper shape can affect positively on the above mentioned

62 drawbacks and so on the costs related to the entire process.[18]

63 Monolithic adsorbents are among the new structured materials – together with fabric structures,

64 foams or laminates – that encountered the attention of the scientific community for gas

65 adsorption, during the last decades.[21-26] They can be characterized by different shapes such as

66 cylindrical, flat plates or block shaped,[1, 27-29] although the honeycomb topology is the one that

67 guarantees the smallest pressure drop thanks to the presence of straight parallel channels

68 extending along the composite body.[21, 25]

69 Among post-combustion carbon capture, electric swing adsorption (ESA) is a process in which

70 the recovery of the adsorbent is obtained by passing electricity through the material,

71 consequentially heated up by means of Joule effect.[21] ESA process can be more effective than

72 TSA if the adsorbent itself is a good electric conductor (e.g. graphitic carbons).[2] In order to

73 obtain a conductive carbon monolith, the easiest and most effective procedure is to prepare a

74 heterogeneous mixture of an active phase and a binder resin and extrude the mixture at high

75 temperatures to give – together with mechanical strength – conductive properties to the final

76 artifact.[1, 17] The production of a monolith is nowadays mainly conducted by the above-cited

77 extrusion method, even though recent works demonstrated the validity of 3D-printing as reliable

78   tool to create structured adsorbents with precise geometries, also at the lab scale.[30, 31] Binder and

79   active phase portions must be carefully chosen because the presence of the former (inert binder)

80   can decrease the efficiency in CO_2 uptake, inducing a gap in the performances of the monolithic

81   adsorbent and the pure active phase. Moreover, the high temperature used for the carbonization

82   of the binder can drastically affect the structure of the active phase. Pore blocking in the active

83   phase due to partial adsorption of the binder could be also not negligible. Because of the

84   different technological readiness levels of a monolith and its corresponding active phase, a

85   comparison among the two is not often possible.

86   The present work reports the performance of a zeolitic active phase (a protonic ZSM-5,

87   MFI framework) and its related monolithic form (78 wt.% H-ZSM-5 / 22 wt.% phenolic resin),

88   to be employed for post-combustion carbon capture. The monolith synthesis occurred at high

89   temperature (800 °C) in order to convert the phenolic resin into a conductive carbon phase. Three

90   samples were considered: the monolith, a powder H-ZSM-5 sample previously subjected to a

91   temperature treatment of 800 °C (H-ZSM-5-800) as in the monolith synthesis and a powder H-

92   ZSM-5 sample that was subjected to the lowest treatment temperature sufficient to remove all the

93   water molecules, that is the one that would be used typically in an academic study on the pure

94   active phase (500°C, H-ZSM-5-500). A multi-technique approach has been adopted in this work

95   in order to cover the most relevant properties of these systems: the structural/compositional

96   properties of both the zeolites and the carbon monolith were evaluated by means of powder X-

97   ray diffraction (P-XRD), surface area analysis, Fourier-transformed infrared spectroscopy

98   (FTIR) and transmission electron microscopy (TEM) coupled with energy dispersive

99   spectroscopy (EDS). Thermal characteristics have been also checked through thermal

100   gravimetric analysis (TGA) and differential scanning calorimetry (DSC).

101 To this set of characterization techniques, the measure of adsorption equilibrium and diffusion of

102 CO_2, N_2, and O_2 at different temperatures was done. The selectivity factors were calculated by

103 exploiting the Ideal Adsorbed Solution Theory (IAST) for a CO_2/N_2 mixture in presence of 5

104 vol.% O_2 to elucidate the CO_2 separation character of H-ZSM-5 and its related monolith. The

105 isosteric heat of adsorption for CO_2, N_2 and O_2 was also evaluated through the analysis of the

106 volumetric isotherms. Water adsorption isotherms were also obtained by means of

107 microgravimetry and the adsorption heat was evaluated by means of microcalorimetry.

108
109

110 **2. Materials and Methods**

111 **2.1 Materials**

112 *H-ZSM-5-500.* H-ZSM-5 sample was obtained by using as precursor the corresponding

113 ammonium form (NH$_4$-ZSM-5, Zeolyst, the Netherlands, product CBV3024E, $SiO_2/Al_2O_3 = 30$,

114 Na_2O 0.05 wt.%, SA 405 m^2 g^{-1}) by heating the zeolite in a tubular furnace up to 500°C in N_2

115 flow (200 ml min^{-1}, ramp rate: 2 °C min^{-1}). The zeolite was kept in isothermal conditions at 500

116 °C for 2 h, and then cooled down to RT with a ramp rate of 3 °C min^{-1}.

117 *H-ZSM-5-800.* H-ZSM-5 sample was obtained by following the same procedure adopted for H-

118 ZSM-5-500, but treating the zeolite at the higher temperature of 800°C, to simulate the

119 conditions encountered by the zeolite in the monolith preparation.

120 *Monolith.* NH$_4$-ZSM-5 precursor was mixed with a phenolic resin (99.5 wt.% in phenol, CAS nr.

121 28064-14-4, Veritas House, Mumbai, India) and subjected to the conventional process given in

122 Scheme 1. During this process, ammonia evolves with temperature and the precursor NH$_4$-ZSM-

123   5 is transformed in the protonic zeolite H-ZSM-5. The final monolith consisted in 78 wt.% of H-

124   ZSM-5 and 22 wt.% of conductive carbon. The monolith was characterized by a conductivity of

125   29 Ω at RT (measured by a multimeter on a 20 cm monolith).

126   The process used to fabricate the monoliths is derived from the extrusion process used for

127   ceramic honeycombs developed as catalyst support for automotive exhaust after treatment

128   systems. Cordierite ceramic honeycombs – together with the extrusion process to mass produce

129   them – have been invented in the mid 1970's to be used as catalytic converters.[32-34]
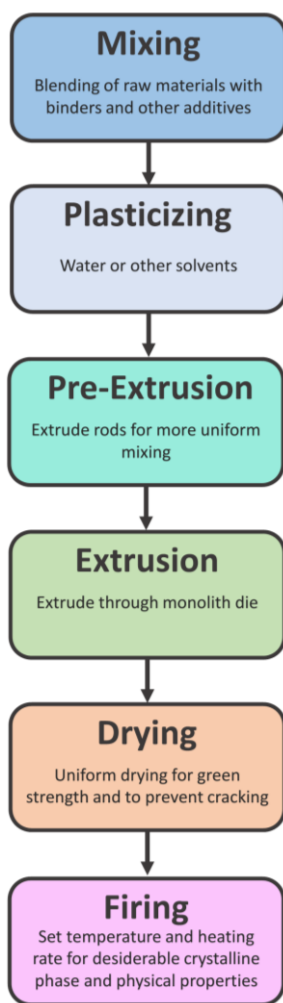
130

131   **Scheme 1.** Conventional process for preparation of extruded ceramic honeycomb monoliths.[35]

132

133   In our case, the slight difference from ceramic honeycombs is that the final firing step is here

134   replaced by a carbonization heat treatment to convert the phenolic resin into carbon. The

135   carbonization temperature is set in a manner that the high surface area of the zeolite is preserved

136   while insuring enough conversion into carbon to obtain the desired electrical conductivity. In this

137   case, ZSM-5 zeolite – which demonstrated a high thermal stability in a preliminary

138   characterization – has been subjected to a carbonization treatment of 800°C in order to achieve a

139   full conversion of the resin into a conductive carbon phase.

140   *Carbon(M).* The pure carbonaceous part of the monolith was obtained by dissolving the monolith

141   in HF to remove the zeolitic part. The undissolved portion was rinsed three times with distilled

142   water before use.

143

144   **2.2 Methods**

145   *FTIR spectroscopy.* In situ FTIR spectra in transmission mode (2 cm^{-1} resolution, average on 32

146   scans) were collected on a Bruker Vertex70 spectrophotometer. The samples were measured in

147   the form of self-supporting pellets inside a quartz cell in controlled atmosphere. Before each

148   measurement the samples were degassed up to 400°C on a vacuum line equipped with a

149   turbomolecular pump ($< 10^{-4}$ mbar). For what concerns the monolith, an aliquot of the powdered

150   monolith was pressed to form a self-supporting pellet. The pellet was then oxidized in 133 mbar

151   of pure O_2 (3 times, 30 min each time) at 500°C and then degassed under dynamic vacuum

152   (residual pressure: 1.0×10^{-5} mbar) at 500°C for 1 h. The integration of the IR peak was

153   performed by fitting each band by using the *Curve fit* utility of OPUS 5.0 program (Bruker Optic

154   Gmbh), and by integrating the area by using the *Integration* utility of the same program.

155   *Volumetry.* N_2, CO_2, and O_2 adsorption isotherms (Table S2-S21 of the Supporting Information)

156   were measured on a commercial volumetric apparatus (Micromeritics ASAP2020). Prior to the

157   measurements, the pure H-ZSM-5 samples (in powder form) and the monolith (in pieces of 0.6 x

158   0.6 x 0.6 cm) were degassed at 400°C on a vacuum line equipped with a turbomolecular pump

159   and then the samples were transferred in the measurement cell in a glove box. Complete set of

160   CO_2, N_2 and O_2 isotherms as recorded up to 1 bar and different temperatures (25, 60, 90 and

161   120 °C for CO_2 while only 25, 60 and 90 °C for N_2 and O_2) are reported in Figure S10 of the

162   Supporting Information. The measurements of surface areas and pore volumes were performed

163   dosing N_2 at 77 K till 1 bar. The $T = 77$ K has been reached by means of a liquid nitrogen bath.

164   Temperature control during the measurements in the RT-90°C range was achieved by using an

165   external isothermal liquid bath (Julabo F25-EH), whereas for the 120°C isotherm an external

166   furnace was used. The specific surface area was obtained by using the Langmuir[36, 37]

167   approximation in the standard pressure range ($0.05 < p/p_0 < 0.20$). Although the BET model is

168   not applicable in the standard pressure range for these materials (negative BET constant), the

169   corresponding surface areas have been reported to allow the comparison with previous studies.

170   Pore size distributions (PSD) were evaluated using the Non-Local DFT (Density Functional

171   Theory) method on the basis of the cylindrical pore model proposed by Tarazona[38] on ASAP

172   2020 V4.00 Software (Micromeritics). The micropore volume (V_{micro}) has been evaluated with

173   the t-plot method adopting the Harkins and Jura equation of thickness in the $0.15 < p/p_0 < 0.50$

174   range.[36] CO_2 (4.8 N, dry bone purity), O_2 (6.0 N) and N_2 (6.0 N) gases were purchased from

175   Rivoira. In section 5.1 of the Supporting Information we reported the Dual and Single-site

176   Langmuir fit calculations for CO_2, N_2 and O_2 isotherms.

177   From the fit of CO_2, O_2 and N_2 isotherms reported in Figure 7a, 7b and 7c, the isosteric heat of

178   adsorption q_{st} has been calculated. Details are reported in section S5.2 of the Supporting

179   information.

180   *Microgravimetric measurements.* Water isotherms (Table S22-S29 of the Supporting

181   Information) were measured by using an intelligent gravimetric analyzer (IGA-002, supplied by

182   Hiden Analytical Ltd, UK), equipped with a fast heating furnace for the temperature control and

183   an ultrahigh vacuum system (10^{-6} mbar). Before each measurement, the samples was degassed

184   for 6 h at 400°C. Buoyancy corrections were carried out using the weights and densities of all the

185   components of the sample and counterweight sides of the balance and the measured temperature.

186   The water isotherms reported in Figure 8 were interpolated by using a cubic spline function. The

187   used skeletal sample density was measured by liquid pycnometry using water (1.74 ± 0.02 g cm^{-3}

188   for H-ZSM-5 and 1.44 ± 0.02 g cm^{-3} for the monolith).

189   *XRD Powder measurements.* X-Ray Powder Diffraction measurements were performed in the 2θ

190   range $2° - 90°$ (step size of $0.0167°$, time per step 200 s) in Debye-Scherrer geometry using a

191   laboratory diffractometer (Panalytical X'Pert Pro Multipurpose Diffractometer) having as source

192   a high powdered ceramic tube PW3373/10 LFF with a Cu anode (Cu Kα: 0.15418 nm) equipped

193   with a Ni filter to attenuate K_β and focused by a PW3152/63 X-ray mirror. The incident beam

194   was collimated by a soller slit (0.04 rad), an antiscatter slit (1/2 Å) and a divergence slit (1/2 Å);

195   for the diffracted beam an antiscatter slit (AS Slit 5.0 mm, X'Celerator) and a soller slit (0.04

196   rad) were adopted. Samples were sealed into boron silica glass capillaries of internal diameter

197   0.8 mm in a protected atmosphere and mounted on a rotating goniometer head.

198   *Differential scanning calorimetry and specific heat capacity.* DSC measurements were

199   performed on the pure active phase (H-ZSM-5-800), on the monolith and on Carbon(M) by

200   heating the sample under N_2 flow at 50 ml min^{-1} by means of a DSC Q200 instrument (calibrated

201   at the melting temperature of indium), from 30 to 200 °C (2°C/min ramp). These measurements

202   were important to evaluate the specific heat capacity (c_p) at different temperatures of the tested

203   materials. This physical quantity can be obtained by the scanning method,[39] as described in

204   Section S3 of the Supporting Information (raw data in Table S1 and Figure S6-S8 of the

205   Supporting Information). For this measurement, the tested materials were activated at 400°C and

206   then inserted each time in a standard aluminum sample holder sealed in controlled atmosphere

207   (Glove Box filled with N_2 5.5 purity grade) in order to avoid adsorption of atmospheric

208   contaminants during the sample loading.

209   Thermogravimetric analysis (TGA) charts have been also conducted on NH_4-ZSM-5 precursor,

210   H-ZSM-500 and the monolith from RT to 900°C in N_2 flow (2°C/min ramp). In the case of the

211   monolith, the flow was switched from N_2 to air for the last hour in order to allow the

212   quantification of the carbonaceous part of the material, as reported in Figure S5, Section S2 of

213   the Supporting Information.

214

215   *Microcalorimetry.* Water adsorption heat was measured at 303 K, with a Tian-Calvet

216   microcalorimeter (Calvet C80, Setaram, France) connected to a grease-free high-vacuum gas-

217   volumetric glass apparatus (residual p $\approx$ 10^{-4} mbar) equipped with a Ceramicell 0-100 mbar

218   gauge (by Varian). The samples were outgassed at 400°C for 6 h. From the heat evolved for each

219   adsorbed amount Δn_a the integral curve $q_{int}(n_a)$ was obtained. The differential heat q$_{diff}$ presented

220   in Figure S16 were obtained by the dose related adsorption heats ($\Delta q_{int}/\Delta n_a$, kJ mol^{-1}) *vs* the

221 middle point of the n_{ads} histogram relative to the individual adsorptive aliquot, prepared as small

222 as possible.

223

224 *TEM/EDS.* Transmission Electron Microscopy analysis was conducted using a JEOL 3010-UHR

225 instrument operating at 300 kV, equipped with a (2k × 2k) pixels Gatan US1000 CCD camera

226 and with an Oxford INCA Energy TEM 200 EDS X-rays analyzer instrument for atomic

227 recognition via energy dispersive spectroscopy (EDS) on the Kα of the elements considered.

228 Quantitative compositional data were obtained using the Oxford INCA Microanalysis Suite

229 software (further details in Figure S4, Section S1.3 of the Supporting Information). For HR-TEM

230 observations, samples where gently milled in an agate mortar. Then, to obtain a good dispersion

231 on the sample holder and avoid any contamination, standard lacey carbon film covered 200 mesh

232 copper grids (Structure Probe, Inc.) were briefly contacted with the powders, resulting in the

233 adhesion of some particles to the sample holders by electrostatic interactions.

234

235 *Pulse and breakthrough measurements.* Diffusion measurements of CO_2, N_2 and O_2 were

236 performed on H-ZSM-5-800 (in form of powder) and on the zeolite–based carbon monolith (in

237 particles having a mesh of 300-500 μm) at 25, 60, 90, 120 °C. While diluted breakthrough

238 experiments were used to determine the diffusion parameters of CO_2, diffusion parameters of O_2

239 and N_2 were determined by pulse chromatography (Figure S11-S16). The experimental

240 conditions of both experiments are listed in Table S30, Section S6 of the Supporting Information.

241 The flow-rate for diluted CO_2 breakthrough curves (0.5 vol.% CO_2 in He from Yara, Norway)

242 was fixed at 20 and 22.5 ml min^{-1} respectively for the feed gas and for the helium used for

243 desorption. Both H-ZSM-5-800 and the final artifact were pretreated at 200 °C under a flow of

244 helium overnight. The calculations for the dimensionless Henry's law constants of CO_2, O_2 and

245 N_2 are listed in Table S31-S36, Section S6.1 of the Supporting Information. Further details on

246 the diffusion of N_2, O_2 and CO_2 are listed in Table S37, Section S6.2 while mathematical model

247 used to simulate pulses and breakthrough curves is presented in Section S6.3 of the Supporting

248 Information.

249

250 *IAST selectivity.* CO_2/N_2 selectivity factors in the presence of 5 vol.% O_2 were evaluated from

251 the CO_2, N_2 and O_2 single component isotherms fitted through a dual site Langmuir equation (see

252 details in Section S5.1) by the Ideal Adsorbed Solution Theory (IAST)[40] using the pyIAST

253 software.[41] Details on the calculation procedure followed for the IAST calculations are reported

254 in Ref. [41]. The dependence of CO_2/N_2 selectivity factors on CO_2 partial pressure for a ternary

255 CO_2 : N_2 : O_2 gas mixture (5 vol.% O_2 gas mixture) at 1 bar and 25, 60 and 90 °C have been

256 obtained for both H-ZSM-5-800 and the monolith by keeping constant the total pressure (1 bar)

257 and the partial pressure of O_2, (0.05 bar) while varying the partial pressure of CO_2 and N_2.

258

259 **3. Results and Discussions**

260 *XRD*. Powder XRD patterns of H-ZSM-5-500, H-ZSM-5-800 and the monolith after activation at

261 400°C are reported in Figure 1. The pattern of NH_4-ZSM-5 – precursor material of the above

262 mentioned H-ZSM-5 zeolite – is also reported for comparison (grey line). In order to obtain the

263 pattern for the monolith, a portion of it was gently grinded in a mortar to preserve the nature of

264 the composite. All the patterns reported in Figure 1 were then normalized to the intensity of the

265 $2\theta = 7.85°$ peak to facilitate their comparison. From the comparison expressed in Figure 1, we

266   can appreciate that the four patterns are very similar. In particular we observe no substantial

267   changes on the samples that incurred on a high temperature treatment (800°C), necessary for the

268   pyrolysis of the resin during the monolith preparation. This result is supported by the well-

269   known resistance of MFI-type zeolites such as ZSM-5 to high temperatures (> 900 °C), because

270   of their low-aluminum content and the absence of Si-O-Si bond angles less than $2\theta = 140°$.[42, 43]

271   The absence of any extra peak and the lack of any peak shift testify also the absence of any phase

272   transition.

273   As the monolith is constituted by 22% of conductive carbon, the presence of an amorphous phase

274   on the black pattern should be observed as broad halos at about 27°, 42° and 78°.[44] At the best of

275   our inspection – based on the black pattern – none of them is observed. In fact, the detection of

276   an amorphous phase and its eventual quantification cannot be evaluated because of the much

277   higher scattering factor of the zeolite with respect to the amorphous one. This fact is confirmed

278   by Figure S3 of the Supporting information, where a comparison between the XRD patterns of

279   the monolith and the phenolic resin carbonized at 800 °C is shown. Moreover, even if detectable,

280   any amorphous phase deriving from the zeolite or from the carbon phase would overlap with the

281   signals arising from the amorphous glass capillary used in the Debye-Scherrer geometry.

14
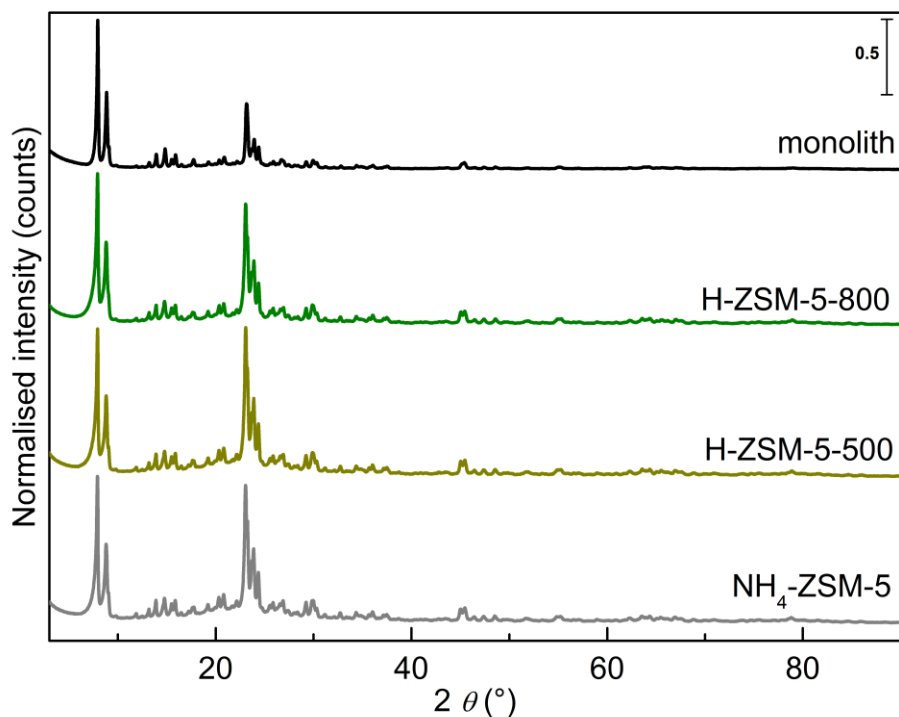
Figure 1. XRPD patterns of NH_4-ZSM-5 precursor in air (grey line) and of H-ZSM-5-500 (dark yellow line), H-ZSM-5-800 (green line) and the monolith (black line), activated in vacuum at 400 °C and kept in inert atmosphere. The pattern intensity has been normalized to the 7.85° peak.

Porosity. Nitrogen volumetry at 77 K is used to evaluate the specific surface area, volume and dimension of the pores of a microporous adsorbent. This type of measurement, performed on a series of samples obtained from different treatment conditions, can help to identify an evolution in the textural properties such as the formation of mesoporosity (appearance of hysteresis loop), pore collapse (substantial decrease in microporosity) or change in particle size (decrease of the external surface area). Nitrogen volumetry has been performed on the above-mentioned set of samples and the results are reported in Figure 2 and Table 1. Nitrogen volumetry at 77 K is

294   known to be a more sensitive technique with respect to XRD to evidence small differences in the

295   structure of materials and in particular eventual structure collapse.[45] Moreover, not asking as

296   prerequisite the crystallinity of the sample, it is able to give indications about the way the

297   structure is modified in terms of surface area, pore volume and dimension, even in the case of

298   sample amorphization. Zeolite structure in general collapses because of too harsh conditions

299   causing its dealumination with the consequential creation of a hierarchical (largely amorphous)

300   pore structure and in particular of mesopores. As it can be seen from the comparison of H-ZSM-

301   5-500 (dark yellow line) and H-ZSM-5-800 isotherms (green lines line) in Figure 2, the textural

302   properties of H-ZSM-5 are not strongly affected when treating the zeolite at 800 °C. In fact, both

303   the zeolites present Ib type isotherms, typical of purely microporous materials,[46] confirming that

304   the samples do not encounter extensive damages in the frameworks. The surface areas reported

305   in Table 1 indicate a decrease in the H-ZSM-800 porosity lower than 10%(experimental error)

306   with respect to H-ZSM-5-500. Pore size distribution analysis does not indicate the presence of

307   mesoporosity for H-ZSM-5-500 and H-ZSM-5-800 samples (see Figure S2b in the Supporting

308   Information), as qualitatively suggested by the shape of the isotherms (type Ib).[46] In the case of

309   the monolith, an increase in the microporosity is observed with respect to H-ZSM-5-800; this

310   fact can be easily related to the presence of the conductive carbon (Carbon(M)). It is interesting

311   to notice that the Carbon(M) phase is characterized by a mesoporous/microporous structures on

312   the basis of the nitrogen volumetric measurements (see blue curve in Figure S2 in the Supporting

313   Information) with a contribution of 624 m^2 g^{-1} of the micropores to the total surface area (1075

314   m^2 g^{-1}) as obtained by the t-plot analysis. By considering that the carbon content in the monolith

315   amounts to 17 wt.% (see Figure S5a), the Langmuir surface area of the carbonaceous phase can

316   be estimated to be 685 m^2 g^{-1}, that is close to the microporous surface area measured for

16

317   Carbon(M) (624 m^2 g^{-1}). Moreover, the N_2 isotherms give some indications about the structure of

318   the carbon: in fact, the hysteresis loop in the monolith isotherm suggests a lamellar structure of

319   the carbon, as expected during the formation of a thin carbon coating on the zeolite surfaces,

320   both on the external and the internal surface.

321
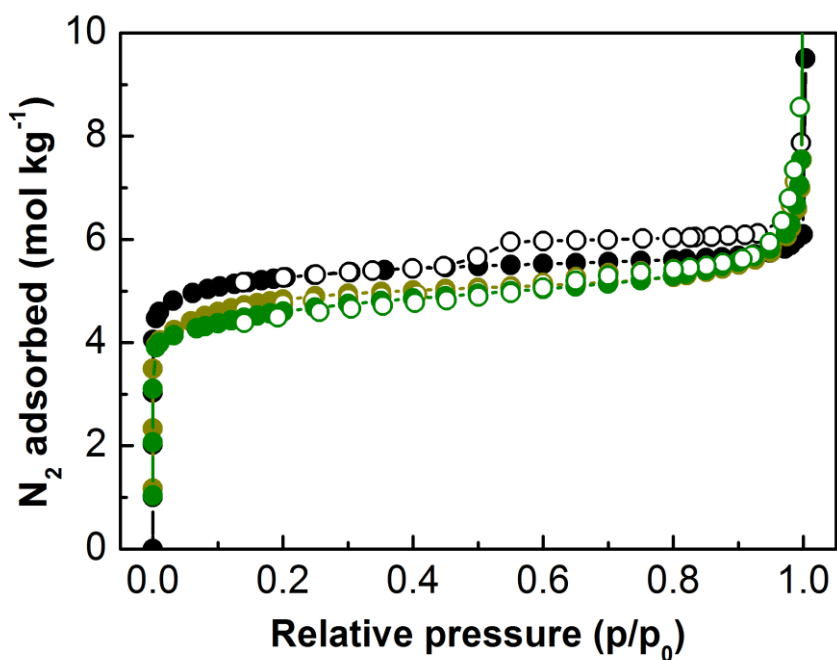
322

323   **Figure 2.** Volumetric N_2 adsorption/desorption isotherms obtained at 77 K for H-ZSM-5-500 (dark yellow curve),

324   H-ZSM-800 (green curve) and the monolith (black curve). Filled and empty scatters refer to adsorption and

325   desorption branches, respectively.

326

327 **Table 1.** BET (S_{BET}, m^2 g^{-1}) and Lanmguir surface areas ($S_{Langmuir}$, m^2 g^{-1}), total pore volume calculated at $p/p_0 =$

328 0.97 (V_{tot}, in cm^3 g^{-1}) and micropore volume (V_{micro}, in cm^3 g^{-1}) of H-ZSM-5-500, H-ZSM-5-800, the monolith and

329 Carbon(M).

|	S_{BET}	$S_{Langmuir}$	V_{tot}	V_{micro}
H-ZSM-5-500	371	492	0.21	0.14
H-ZSM-5-800	350	467	0.21	0.13
monolith	397	528	0.20	0.16
Carbon(M)	801	1075	0.72	0.30

330

331 *TEM*. High resolution transmission electron microscopy (HR-TEM) was used to evaluate the

332 interaction between zeolite particles and the carbonaceous phase, and detect possible

333 modifications occurred to the inorganic phase (zeolite) during the extrusion process. Microscopy

334 allows also visualizing the carbon structure in the monolith. For what concerns H-ZSM-500 and

335 H-ZSM-800, because of the coincidence of the results obtained for the two systems, only the

336 results concerning H-ZSM-5-800 have been reported in the following. Synoptic views of the H-

337 ZSM-5-800 material and of the monolith are displayed in Figure 3, parts (a,) and (b, c),

338 respectively.

339 At low magnification, the TEM images showed that the projections for both the H-ZSM-5-800

340 (Figure 3a) and the monolith (Figure 3b and c) particles are similar, exhibiting irregular

341 polygonal shapes, with size ranging from some tens to some hundreds of nm (see section S1.3 of

342 the Supporting Information, Figure S4d and S4e). For the monolith , two images are reported as

343 an example of a number of cases of i) the zeolite almost completely un-blended from the carbon

344 phase (Figure 3b) – even after the gently manual milling – and ii) the zeolite still blended

345   together with the carbon phase (Figure 3c). Concerning the latter, it is worth noticing that zeolite

346   grains (yellow dashed line in Figure 3c) and carbon (orange dashed line in Figure 3c) appeared in

347   quite close contact, with the carbonaceous phase exhibiting the aspect of small flakes which, on

348   the basis of the very pale contrast, might be as thin as a layer few atoms thick. This observation

349   confirms what expected from the shape of the monolith N_2 isotherms (black line, Figure 2) and,

350   on the basis of the XRD results, suggesting a very high dispersion of the carbon. At higher

351   magnification, for both samples the particles exhibited lattice fringes with similar frequency

352   (Figure S4b and S4c), witnessing the crystallinity of the object inspected, and confirming – at the

353   microscopic level – the XRD and N_2 volumetry results presented in the previous section that is

354   the persistence of the crystalline character for the zeolite particles in the monolith.

355
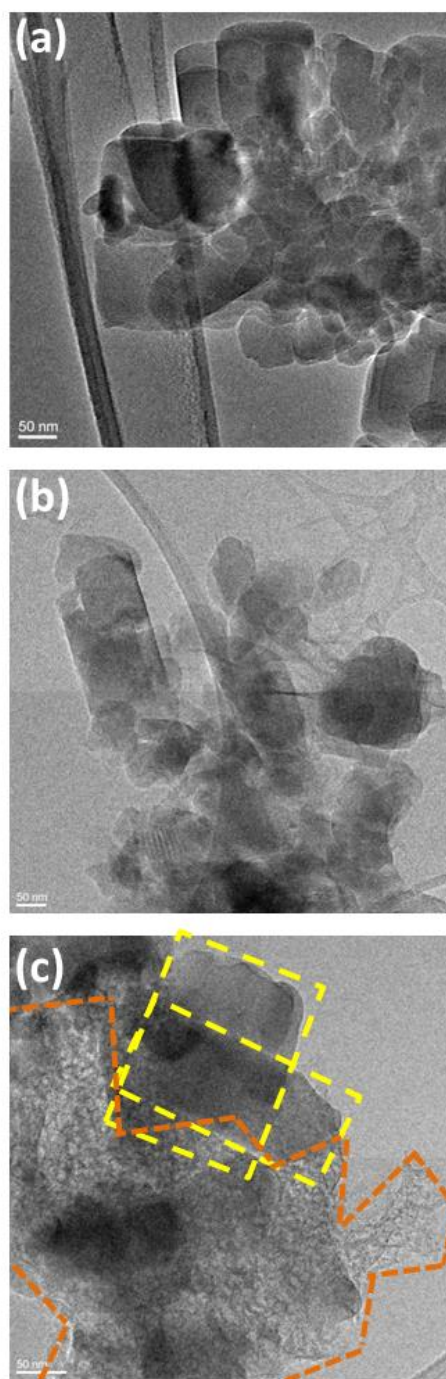
Figure 3. TEM images (original magnification = 30k x) of: (a) H-ZSM-5-800; portions of the monolith showing the zeolite and the carbonaceous part (b) unblended or (c) blended together. In part c, zeolite particles are traced with yellow dashed line while the carbon flakes are traced with orange dashed line.

359

360   An EDS analysis of the monolith was carried out, collecting data for both particles and ensemble

361   of particles surrounded by the carbonaceous phase (e.g. Figure 3c), and for particles un-blended

362   from it (e.g. Figure 3b). To obtain statistically reliable data, the number of particles analyzed was

363   increased until the invariance in the distribution of the results was attained (reported in Figure 4

364   Figure 3). This resulted in the collection of ca. 300 analyses for each group. Sodium was the only

365   extra element found with respect to those constitutive of H-ZSM-5, i.e. Si, Al, and O (besides C).

366   Sodium was present in the phenolic resin and this result indicates that Na^+ ions diffused within

367   the zeolite channels during the monolith synthesis partially exchanging H^+. Its content was

368   evaluated in terms of Na/Al atomic ratio, in order to evaluate the degree of the cation exchange.

369

370
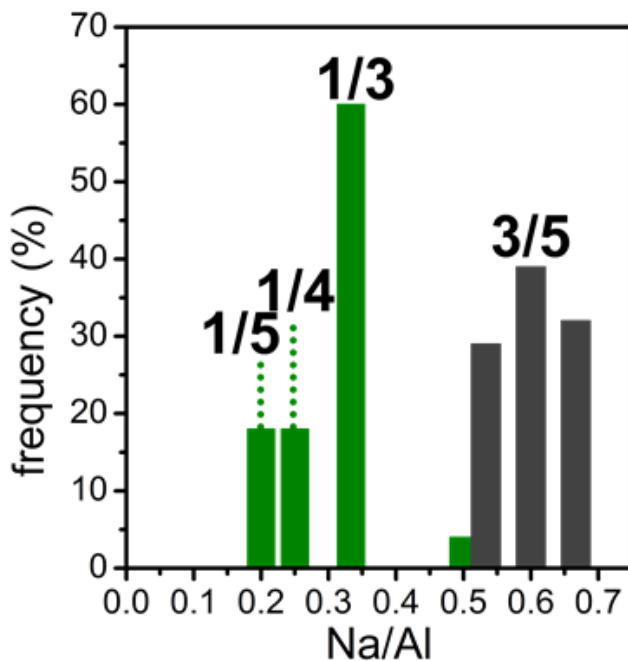
371   **Figure 4.** Distribution histograms of the Na/Al atomic ratio in the monolith. Green bars: zeolite particles almost

372   separated from the carbon (e.g. like in Figure 3 part b); grey bars: zeolite particles still embedded in the carbon (e.g.

373   like in Figure 3 part c).

374

375   Figure 4shows the distribution histograms of the Na/Al values resulting from the analysis of the

376   zeolite particles surrounded by carbon (grey bars) or (almost) unblended from it (green bars).

377   Focusing on these latter, basically a Na/Al = 1/3 was overwhelmingly found, while the ratio

378   appeared higher when analyzing zeolite particles and carbon still mixed together, witnessing for

379   the presence of Na^+ in the carbonaceous phase.

380

381   *FTIR.* As well known, TEM −as all other types of microscopies − suffers from the limitation of

382   the extremely small amount of sample analyzed (typically, nanograms). Moreover, diffraction

383   and volumetry are not sensitive to small changes in the chemical nature of the sample.

384   Confirmatory evidence of the exchange of original H^+ with Na^+ in zeolitic part of the monolith

385   was sought by IR spectroscopy. In fact, hydroxyl stretching frequency $\nu(OH)$ is strongly

386   dependent on the chemical environment of the −OH species and to their acidity. It is then easy to

387   differentiate the protons of i) Brønsted sites (Si-OH-Al, 3615 cm^{-1}) ii) the −OH associated to

388   defect species, i.e. silanols and iii) the −OH associated to extraframework Al^{3+} due to partial

389   dealumination. In our case, the latter might be generated from the high temperature necessary for

390   the monolith preparation (Al-OH, 3670 cm^{-1}). A pictorial representation of H-ZSM-5 structure

391   and of the different, possible hydroxyl species is reported in Figure S1. Among all these species,

392   Brønsted sites are the ones characterized by the higher electrostatic potential and then represent

393   the preferential adsorption sites for incoming molecules as CO_2. A preservation of the structure

394   and of the concentration of the zeolitic counterions is important in order to preserve the affinity

395   of the zeolite toward CO_2 also in the monolith. On the other hand, a cation exchange of the

396   protons with Na^+ suggested by EDS, is expected to cause an increase in the CO_2 affinity with

397 respect to the pure zeolitic form, on the basis of results previously reported for H-ZSM-5 (ΔH_{CO2}

398 $= 31.3$ kJ mol^{-1}, Si/Al $= 11.5$)[47] and Na-ZSM-5 ($\Delta H_{CO2} = 50.0$ kJ mol^{-1}).[47] In Figure 5, the

399 spectra obtained for H-ZSM-5-500 (dark yellow line) and H-ZSM-5-800 (green solid line) are

400 reported. In the H-ZSM-5-500 spectrum, the predominant species are the H$^+$ counterions,

401 doubling in intensity the silanols species signal and with only minor contributions associated to

402 extraframework Al^{3+}. The absence of open extralattice Al (i.e. coordinative unsaturated, highly

403 reactive Al^{3+} sites), was indicated by infrared vibrational characterization at 77 K through N$_2$

404 (results not reported in this manuscript), a molecular probe able to detect also very low amount

405 of open Al^{3+} sites.[48] Interestingly, also for H-ZSM-5-800, Al^{3+} was not detected by N$_2$,

406 confirming what expected on the basis of TEM, XRD and N$_2$ adsorption results, that indicated

407 only minor effects on the structure deriving from the thermal treatment. Conversely, the

408 comparison of the IR spectra in the ν(OH) region, shows quite a substantial change of the IR

409 profile upon the treatment at 800 °C (see green solid curve in Figure 5). The silanols band

410 becomes slightly sharper, whereas the signal related to Al-OH doubles in intensity with a

411 corresponding decrease of the band related to the strong Brønsted sites. In particular the latter is

412 halved with respect to H-ZSM-5-500, testifying the relevant disappearance of some of the sites

413 that should give preferential interaction towards CO$_2$. A decrease in the Brønsted sites

414 concentration was suggested also by thermogravimetric analysis on the zeolite where a weight

415 loss was detected over 500 °C (see Figure S5b of the Supporting Information), a temperature

416 where molecular water should not be present anymore. This loss is associated with the partial

417 delamination of the framework, requiring a decrease of the protons concentration.

418
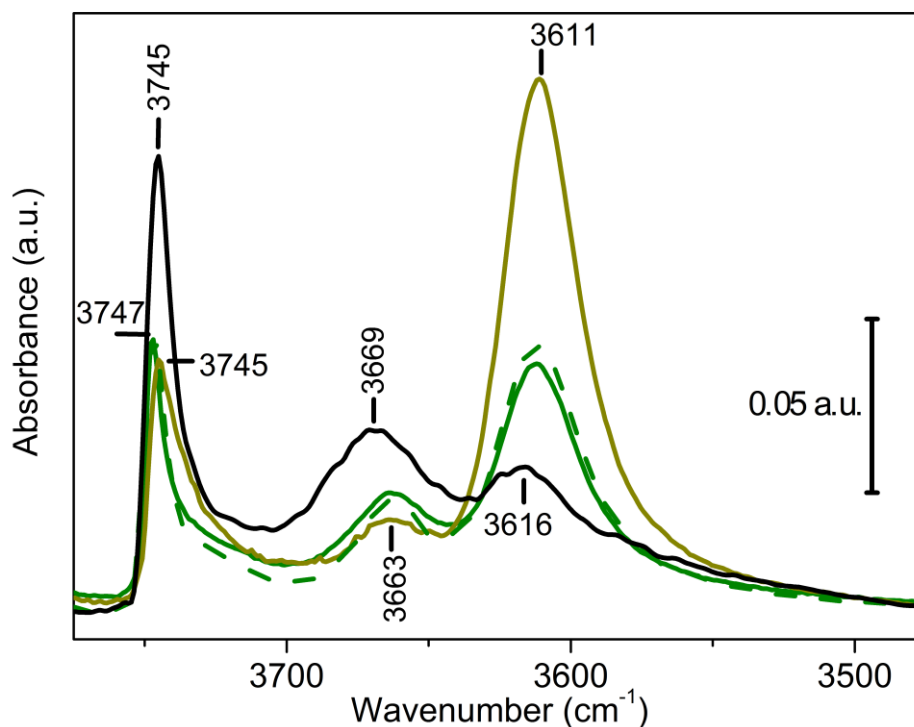
Figure 5. (a) IR spectra of H-ZSM-5-500 (dark yellow line) and H-ZSM-5-800 (green, solid line) in vacuum at RT, after activation at 400°C. It is evident that the intensity of the 3614 cm^{-1} band (related to the strong Brønsted sites) is halved in the H-ZSM-5-800 with respect to the H-ZSM-5-500. The IR spectrum of the monolith recovered from the pyrolysis in O_2 flow of the carbonaceous part (black curve). The spectrum of the H-ZSM-5-800 (green, dotted curve) after a similar treatment is also reported for comparison. All the spectra were normalized with respect to a characteristic pattern in the 2200-1600 cm^{-1} range, due to combination and overtone of vibrational modes of the framework, the intensity of which is then proportional to the amount of sample investigated by the IR beam. The spectra were baseline subtracted by using as baseline a straight line passing for the two extremes of the frequency range reported in the plot.

The monolith was not transparent to the mid-IR radiation because of the presence of conductive carbon. For this reason, before the analysis, the sample was treated in O_2 flow at 500°C in order to pyrolize the carbon: the corresponding spectrum is reported as black curve in Figure 5. For the sake of comparison, the same procedure was repeated on H-ZSM-5-800: the corresponding spectrum (P) is reported as a green dotted line in the same figure. The area of the three main peaks in the OH stretching region for these two samples is reported in Table 2.

436

Table 2. Position, integrated area and relative changes of relevant ν(OH) bands in the IR spectra of H-ZSM-5-800 (P) and ZSM-5 recovered from the monolith (M). Both the sample were calcinated in O_2 at 500°C before the spectrum recording.

| Position (cm⁻¹) | Assignment | Integrated area (a.u. cm⁻¹) | | Ratio | |
		H-ZSM-5-800 (P)	monolith (M)	P/M	M/P
3745	Si-OH	1.25	2.21	0.56	1.78
3665	Al-OH	1.11	2.42	0.45	2.20
3614	Si-(OH⁺)-Al	3.12	2.12	1.48	0.67

440

It is evident that, although the treatment in O_2 is not able to further affect the H-ZSM-800 spectrum (as demonstrated by the comparison of the solid and the dotted green lines in Figure 5), the band associated to the Brønsted sites is significantly decreased in intensity in the monolith (black line, Figure 5). From the values reported in Table 2, the integrated intensity of this band decreases of about 1/3. The decrease in the proton concentration in the monolith cannot be restricted to dealumination only. TEM/EDS data are thus fully confirmed, suggesting a cation exchange by Na^+ during the monolith synthesis. The IR spectrum of the zeolitic part of the monolith suggests also that the processing for the fabrication of the monolith should have affected in some extent also other parts of the zeolite framework, because an increase of Al-OH and Si-OH defect sites is observed with respect to H-ZSM-5-800. Being these modifications significantly larger with respect to H-ZSM-800(P), it can be inferred that they are related to the

452   chemical environment created by the decomposition of the phenolic resin and not simply to the

453   high temperature conditions required by the pyrolysis.

454   *Specific heat capacity.* The specific heat capacity c_p is an important parameter for a material to

455   be used for carbon capture purposes.[3] In fact, when the regeneration of the adsorbent is done by

456   temperature (TSA), the energy required for this step will be directly related to the heat capacity

457   of the material. Water heat capacity (4.18 kJ kg^{-1} °C^{-1}) is considered a reference c_p value, being

458   the main component of amine-based scrubbers,[49] nowadays the state-of-the-art technology for

459   post-combustion CO_2-capture.[5] Water is characterized by a very high heat capacity and its use as

460   solvent in these systems is at the basis of the high energy penalty paid in the carbon capture

461   chain. On the other hand, a too low heat capacity can facilitate the creation of hot spots in the

462   material causing its fast degradation.[5] In Figure 6, the specific heat capacity of H-ZSM-5-800 (1,

463   green line) and of the monolith (3, black line) are reported as a function of the temperature and

464   compared to those of other solid sorbents proposed for CO_2-capture technique. The c_p obtained

465   for the pure carbonaceous phase is also reported (2, dark cyan). Details on c_p measurements are

466   reported in Section S3 of the Supporting Information. The zeolite and the composite showed

467   totally different values and dependence of c_p on temperature. The pure zeolitic material (H-ZSM-

468   5-800) has a c_p value of 0.8 kJ kg^{-1} °C^{-1}, almost independent on temperature, in the 60-140°C

469   range. The presence of the carbon coating has two main effects: (i) an increase in the c_p values

470   (from 0.8 to 1.1 kJ kg^{-1} °C^{-1}, at 60°C) and (ii) a strong dependence of c_p on the temperature. For

471   what concerns point (i), this can be related to a larger degree of freedom for the molecules within

472   the carbonaceous phase with respect to the one of the zeolite phase, as explained by Mu et al.[50]

473   The dependence highlighted in point (ii) can be generally explained through the definition of

474   heat capacity, i.e. a constant that regulates the proportionality between the internal energy of a

475   material and the temperature applied: whenever extra degrees of freedom (such as rotation and

476   vibrations quantized energy modes) are induced in the constituent molecules of a material, the

477   internal energy increases and so does the constant c_p. in order to maintain the proportionality

478   between temperature and internal energy, as explained by the equation S1 in section S3 of the

479   Supporting Information.

480   This can be the case of carbonaceous phases. In fact, as reported in Figure 6, the c_p trend (slope)

481   of Carbon(M) is reassembled by other another carbonaceous material such as double-walled

482   carbon nanotubes (DWCNTs).

483   Although the heat capacity contribution of the carbonaceous phase leads to a higher c_p in carbon

484   monolith with respect to the one of zeolite active phase alone (black triangles line vs. green

485   triangles line of Figure 6), the c_p values obtained for the structured adsorbent are still in the range

486   considered interesting for practical applications being only one fourth of that of aqueous

487   solution. To confirm this statement, we reported in Figure 6 the heat capacity of interesting

488   materials for CO_2 capture such as MOF-177,[50] UTSA-16,[12] NaX[51] and Zeolite 4A.[52] In fact, the

489   PSD curve (see Figure) do not evidenced the presence of mesopores also in the monolith.


490
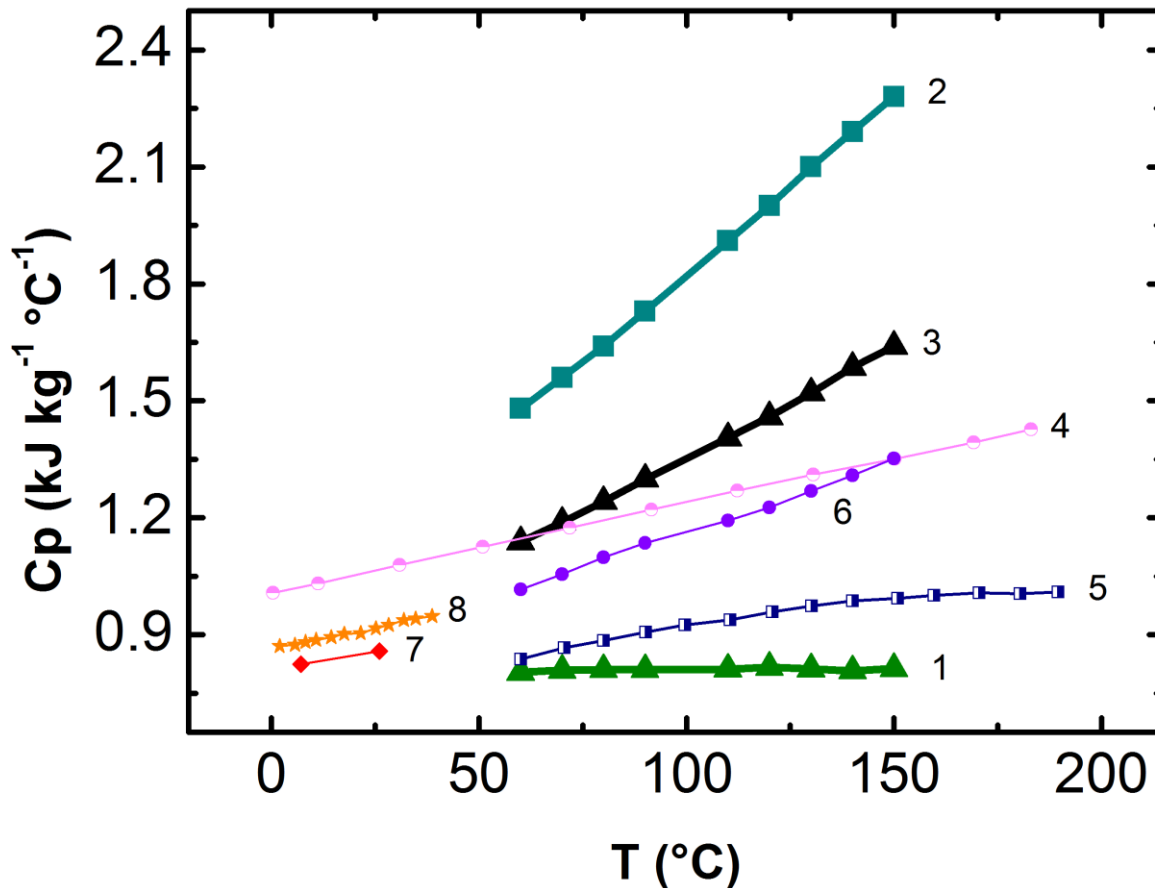
Figure 6. Specific heat capacities of H-ZSM-5-800 (1, green, full triangles, this work), Carbon(M) (2, dark cyan, full squares, this work), carbon monolith (3, black line, full triangles, this work) and of materials proposed for CO_2-capture in the literature: DWCNT (4, light pink line, half circles),[53] MOF-177 (5, blue line, half squares),[50] UTSA-16 (6, violet line, circles),[12] NaX (7, red line, rhombi),[51] Zeolite-4A(8, orange line, stars).[52]

CO_2, O_2, N_2 and H_2O capacity. In order to test the CO_2 affinity of the monolith with respect to its parent material (H-ZSM-5), a series of CO_2, N_2, O_2 volumetric adsorption measurements has been recorded at pressure range 0-1 bar and within the temperature range of interest (25-120°C). These isotherms have been reported in Figure 7a. The results obtained on H-ZSM-5-500 and H-ZSM-5-800 were fully comparable for all the adsorbates considered at RT (see Figure S9 in the Supporting Information). For this reason, the full volumetric characterization was performed only for H-ZSM-5-800.

504
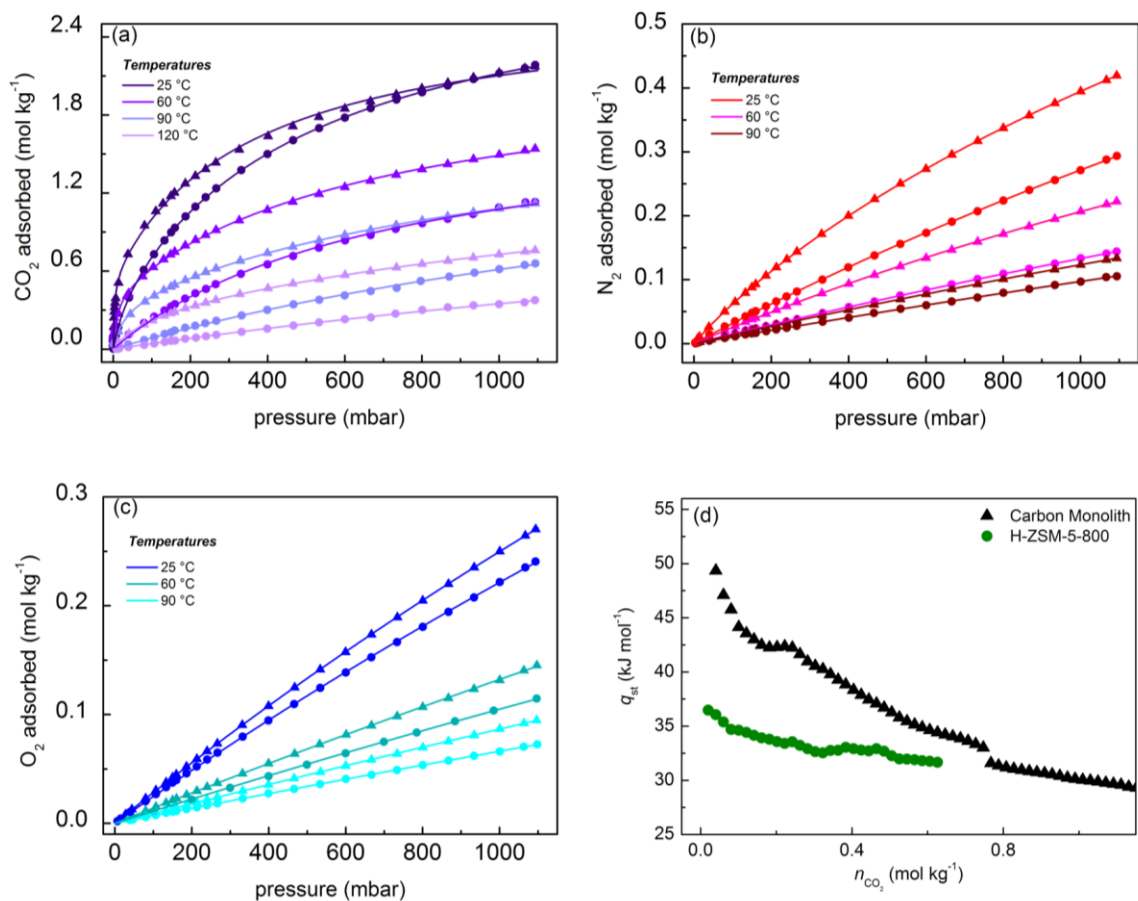
Figure 7. (a) CO_2, (b) N_2 and (c) O_2 adsorption isotherms on H-ZSM-5-800 (●) and the monolith (▲) at 25, 60 and

90 and 120 °C (at 120 °C only for CO_2. CO_2 color code: from dark violet (25 °C) to light violet (120 °C). N_2 color

code: red (25 °C), magenta (60 °C) and dark red (90 °C). O_2 color code: blue (25 °C), dark cyan (60 °C) and cyan

(90 °C). Desorption branches are reported in Figure S10 of the Supporting Information. Continuous lines has been

obtained from the Dual and Single-site Langmuir fits (details are listed in section S5.1 of the Supporting

Information) (d) CO_2 isosteric heat of adsorption calculated by fitting the isotherms reported in part (a) for H-ZSM-

5-800 (green scatter) and the monolith (black scatter). The q_{st} has been calculated up to the coverage that allowed

the fit of at least 3 points (details of q_{st} calculation are listed in section S5.2 of the Supporting Information).

513

For what concerns CO_2, a capacity of 2.2 mol kg^{-1} was obtained at 25°C and 1.1 bar for both the

monolith (triangles in Figure 7a) and the H-ZSM-5-800 (circles); nevertheless a different shape

29

516   of the isotherms can be noted, suggesting a higher affinity toward CO_2 of the monolith, being the

517   CO_2 capacities higher for the latter at $p \leq 0.2$ bar, which the typical partial pressure range for

518   CO_2 in a post-combustion flue gas. This is particularly interesting because it shows how the

519   adsorption properties of a material would be underestimated if evaluated on the basis of the pure

520   active phase alone; it is then important to study the adsorption characteristic of an adsorbent

521   which was previously molded in a shape as close as possible to the one that will be actually

522   employed. The gap in the adsorption properties between the pure active phase alone and the final

523   artifact (i.e. zeolite-based carbon monolith), is even more pronounced when we consider the

524   curves obtained at higher temperatures (as illustrated the curves of lighter violet in Figure 7a). In

525   fact, for higher temperatures, a larger CO_2 uptake is observed along the whole isotherm for the

526   monolith with respect to H-ZSM-5-800. The explanation of this behavior can be associated to the

527   fact that, as described in the previous section, upon the preparation of the honeycomb, some Na^+

528   replaced protons in the pristine H-ZSM-5 giving rise to the formation of a H-Na-ZSM-5, where

529   Na can exert a higher electric field towards CO_2 than protons (4.8 vs. 3 V nm^{-1}).[54] In addition to

530   the presence of Na^+ (replacing some H^+), also the presence of a higher amount of local defects

531   (increase of silanols) and partial extra framework OH groups, could give some beneficial effect

532   to the adsorption properties of the final material.

533   Figure 7b and c show N_2 and O_2 adsorption isotherms at 0-1 bar and different temperatures for

534   both H-ZSM-5-800 (circles) and the monolith (triangles). Despite the fact that the adsorbed

535   quantities of these gases are much lower than those registered for CO_2, the higher N_2 (or O_2)

536   uptake of the monolith with respect to H-ZSM-5-800 is still remarkable. As this affects the

537   selectivity factors in the two samples was evaluated with the Ideal Adsorbed Solution Theory

538   (IAST) analysis (see below).

539   Water is one of the components of the flue gases that largely affects the CO_2 adsorption

540   properties of a material. In fact, water is preferentially adsorbed by materials, lowering the CO_2

541   storage properties. Increasing the material hydrophobicity is a strategy to improve its CO_2-

542   captureperformances in presence of a real flue gas flow. Gravimetric adsorption isotherms of

543   water are reported in Figure 8 for H-ZSM-5-800 (part a) and the monolith (part b) from 25 to 120

544   °C and partial pressure up to 22 mbar at 25°C and 45 mbar for $T > 25$°C.

545
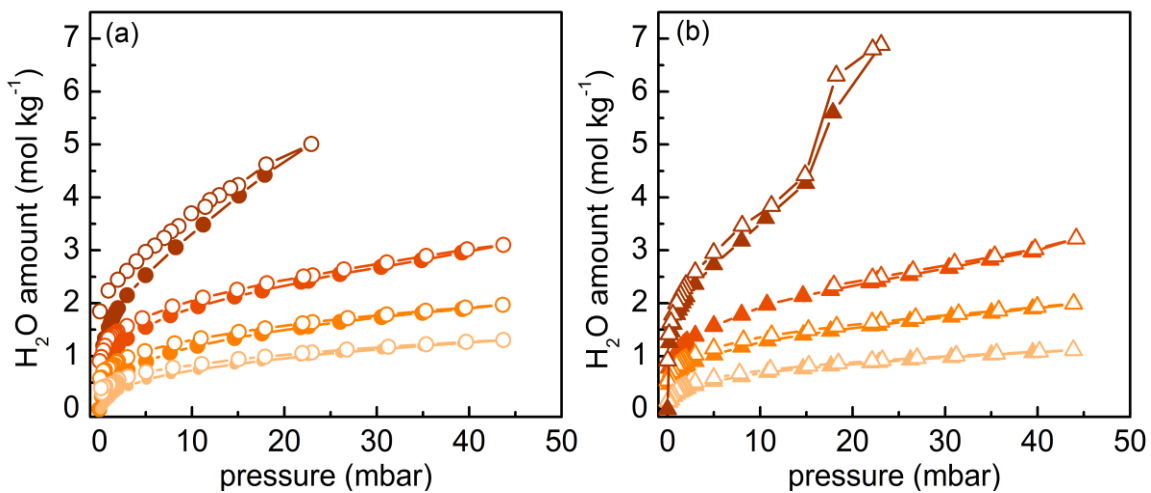
547   **Figure 8.** H_2O adsorption (full dots) and desorption (empty dots) isotherms of H-ZSM-5-800 (a) and the monolith
548   (b) at 25, 60, 90 and 120 °C. Color code: from dark orange (25 °C) to light orange (120 °C).
549

550   From the comparison between the two samples it is evident that the presence of the carbon has

551   two main effects on the water adsorption isotherm: (i) change in the adsorption capacity; (ii)

552   change in the shape of the isotherm. These two effects are different at the different temperatures

553   because of the different p/p_0 ranges considered ($p_0 = 0.7$, 0.2, 0.08 and < 0.04 at 25, 60, 90 and

554   120°C respectively). For what concerns the 90 and 120°C isotherms, a lower capacity is verified

555   for the monolith with respect to the zeolite. On the contrary, in the 25 and 60°C isotherms, the

31

556 maximal water capacity is increased in the monolith with respect to the zeolite. Moreover, also

557 the position and shape of the hysteresis loop is significantly different: a "S" shaped upper curve

558 related to water capillary condensation within the carbon framework pores is visible for the

559 monolith recalling the typical isotherm shape of activated carbons. The relative pressure α at

560 which half of the total water capacity is reached in a material is a good indicator of the

561 hydrophobicity of such a material;[55] the higher is this value the higher will be the hydrophobic

562 character. The total water capacity was estimated from the material micropore volume to 7.8 and

563 16.8 mol kg^{-1}, for H-ZSM-5-800 and the monolith, respectively. α would correspond to 12 mbar

564 for H-ZSM-5-800, whereas it would be definitely larger for the monolith (outside the pressure

565 range considered), characterized by a larger hydrophobicity. The hysteresis loop closes at about

566 15 mbar for the monolith, whereas it closes at pressure lower than 1 mbar in the case of the

567 zeolite suggesting as the presence of the carbon would facilitate the complete reactivation of the

568 material upon degassing. Another important point is related to the dependence upon temperature

569 of the isotherms in the two materials: in fact, as mentioned above, since the water capacity is

570 lower for the monolith than for H-ZSM-5-800 at 90 and 120°C, a larger working capacity is

571 expected for the monolith by reactivation upon thermal heating. This datum is quite meaningful

572 in terms of post-combustion CO_2-capture where H_2O is present in 5-7 vol.%.[33] The material

573 affinity for water was also evaluated by means of microcalorimetric measurements (see Figure

574 S17). Accordingly, the heat of adsorption in the zeolite (121 kJ mol^{-1}) is 20% higher than in the

575 monolith (96 kJ mol^{-1}). These values are close to those previously reported for ZSM-5 zeolites.[56]

576 Literature values always indicate a lower water affinity for Na- than for H-ZSM-5,[56] suggesting

577 that not only the presence of the carbonaceous phase, but also the H^+ to Na^+ exchange

578 contributes to the increased hydrophobicity of the monolith.

579 *Diffusion measurements. Breakthrough and pulse chromatography measurements.*

580 In gas adsorption, the Henry's law constant (K_H) is defined as another way to establish the

581 affinity of an adsorbate towards an adsorbent surface. In this study, K_H has been evaluated for

582 CO_2, N_2 and O_2 by means of diluted breakthrough (Figure 9a) and pulse chromatography

583 experiments (Figure 9b,c) for both H-ZSM-5-800 and the monolith. These measurements were

584 performed in the 25-120 °C temperature range, analogously to the static volumetric

585 measurements (see Section 6 of the Supporting Information).

586
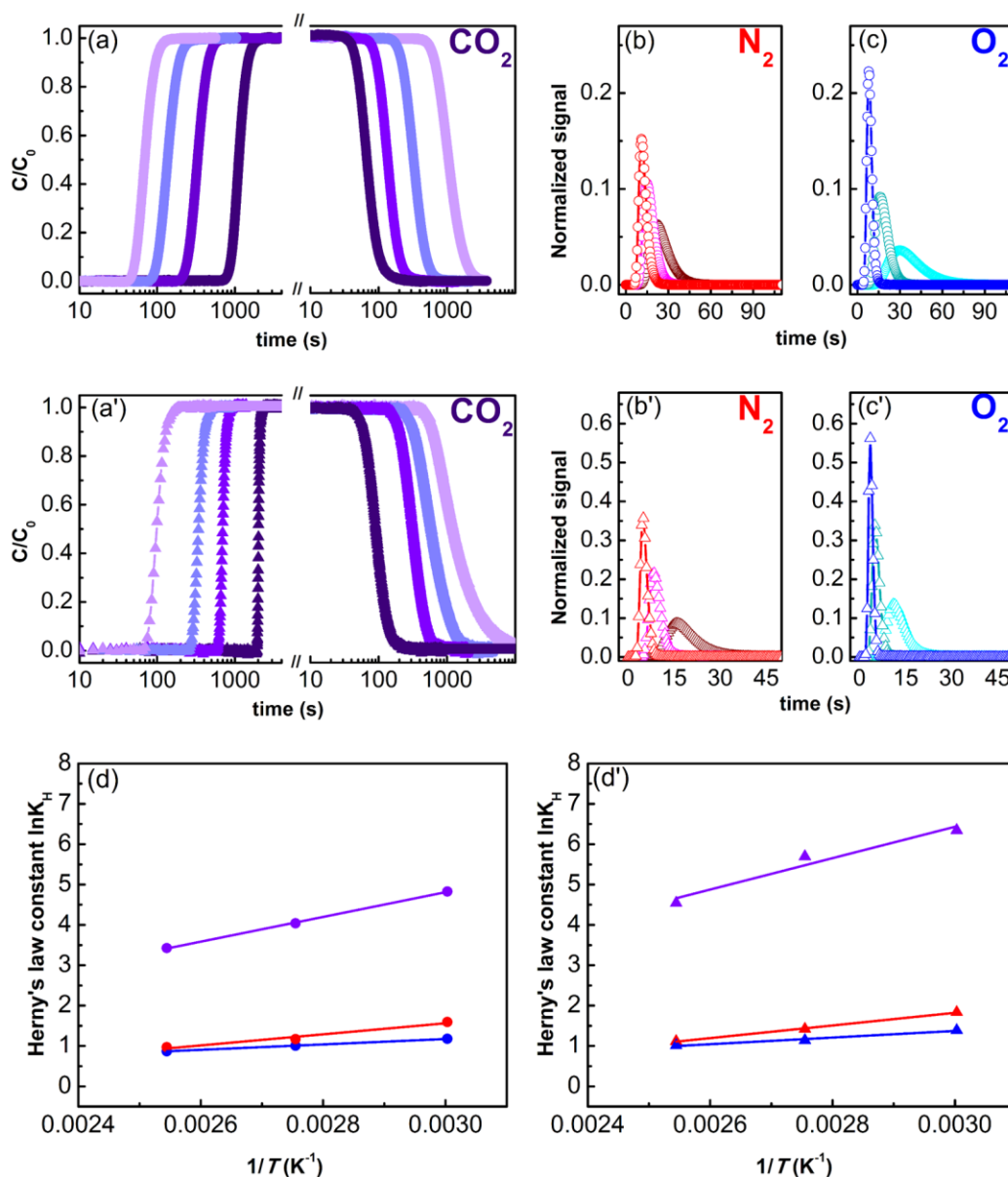
Figure 9. Experimental CO_2 breakthrough adsorption/desorption curves (0.5 vol.% CO_2 in He) on (a, ●) H-ZSM-5-800 and (a', ▲) the monolith at 25, 60, 90 and 120 °C. Color code: from dark violet (25 °C) to light violet (120 °C). X-axis is reported in logarithmic scale. Experimental (symbols) and model (continuous line) data for N_2 and O_2 pulse chromatography on (a' and a'') H-ZSM-5 and on (b' and b'') the monolith at 60 °C. The pulse chromatography curves show the signal dependence of the flow: 10 (blue for O_2 and red for N_2), 20 (cyan for O_2 and magenta for N_2) and 30 ml min^{-1} (dark cyan for O_2 and wine for N_2). The natural logarithm of the Henry's law constant K_H is plotted against 1/T for H-ZSM-5 (d, ●) and for the monolith (d', ▲) in the T range 60-120 °C. K_H has been evaluated for CO_2 (violet), N_2 (red) and O_2 (blue). Symbols refer to experimental points while continuous line represents the linear fit.

34

598   Figure 9d and Figure 9d' represent the variation of lnK_H with respect to $1/T$, for H-ZSM-5-800

599   and the monolith respectively. As expected, the K_H values decrease with the increasing of the

600   temperature. Furthermore, focusing on the Tables S31 to S36 in the Supporting Information, we

601   can notice how K_H for CO_2 are at least one order of magnitude higher than those of N_2 and O_2

602   testifying the higher affinity of both H-ZSM-5 and the monolith to CO_2 with respect to N_2 and

603   O_2. The affinity of CO_2 towards the adsorbent is evidently higher in the case of the monolith than

604   for H-ZSM-5 pure active phase: this result is in line with the presence of Na^+ cations, as

605   previously discussed in the TEM/EDS and FTIR section.

606   Breakthrough and pulse chromatography experiments were also useful to evaluate the diffusivity

607   of CO_2, N_2 and O_2 within H-ZSM-5-800 pure active phase and the monolith. The diffusivity

608   parameters obtained are listed in Table S37. It is interesting to notice that the diffusivity

609   parameters of CO_2, N_2 and O_2 are very high for both the H-ZSM-5-800 and the carbon monolith.

610   The fast diffusion of CO_2 is an important feature in view of an employment of these materials for

611   real applications. A promising material for CO_2-capture in which similar values of diffusivity

612   were obtained is UTSA-16 (0.015 s^{-1} at 60 °C).[57]

613

614   **4. Discussions**

615   *Isosteric heat of adsorption.* To evaluate the relative affinity of CO_2, N_2 and O_2 for the monolith

616   and H-ZSM-5-800, the isosteric heat of adsorption has been calculated (details reported in

617   section 5.1 if the Supporting Information). The values obtained at the lowest coverage, which

618   represent the interaction of the adsorbates with the strongest interaction sites, are reported in

619   Table 3. These values have been obtained from the adsorption isotherms reported in Figure 7a,

620   6b and 6c, respectively.

621   For what concerns CO_2, the isosteric heat calculated for H-ZSM-5-800 is close to the one

622   reported previously for H-ZSM-5 by Dunne et al. (ΔH_{CO2} = 38.0 kJ mol^{-1}, Si/Al = 30).[54] For the

623   monolith, an isosteric heat significantly higher than that of H-ZSM-5-800 is obtained.

624   Interestingly, this value is close to the adsorption enthalpy reported in the literature for Na-ZSM-

625   5 (ΔH_{CO2} = 50.0 kJ mol^{-1}),[47,54, 58] confirming the ion exchange hypothesized on the basis of the

626   EDS and IR spectroscopies results. In Figure 7d, the dependence of the CO_2 q_{st} on the coverage

627   is also reported. Supposing that the initial Si/Al = 30 ratio is maintained in the zeolite structure,

628   the full coverage of the counterions with the formation of 1:1 adduct is expected at 1.39 mol kg^{-1}

629   in H-ZSM-5-800 and 1.08 mol kg^{-1} in the monolith. The curves in Figure 7d suggest that the H-

630   ZSM-5-800 sample is characterized by a large homogeneity of the adsorption sites, whereas the

631   monolith surface is largely heterogeneous. The presence of sodium as counter-cation,

632   accompanied by the increase of silanols and partial extra-framework aluminum observed in the

633   monolith, leads to a higher chemical interaction towards CO_2 than the one registered for H-ZSM-

634   5-800 where the role of counter cation is played only by protons, and a lower amount of silanols

635   and partial extra-framework aluminum sites are present.

636   In particular, an estimation of the degree of the H^+ to Na^+ exchange can be inferred from this

637   graph in about 0.25 mol kg^{-1}, i.e. one fourth of the total counterions, This result is in agreement

638   with what found by means of IR and EDS spectroscopies, allowing then to describe the zeolitic

639   phase in the monolith as a highly defective H-Na-ZSM-5.

640   The N_2 heat of adsorption on H-ZSM-5-800 is instead slightly lower than the energetic value

641   reported in the literature by means of variable temperature IR methods (19.7 ± 0.5 kJ mol^{-1} on H-

642   ZSM-5 and or 20 ± 1 kJ mol^{-1} on H-FER)):[59, 60] this fact can be related to the different way the

643   two methods allow the adsorption affinity determination. Methods based on IR are site specific:

644   in particular, in this case only the energetics of the most energetic surface sites (protons) was

645   considered. For what concerns the isosteric heat, it can be seen as an average on all the sites

646   contributing to the interaction at a certain pressure.

647   For what concerns the O_2 isosteric heats obtained for both the zeolite (14 kJ mol^{-1}) and the

648   monolith (15 kJ mol^{-1}), the values are close to the adsorption heat reported for other zeolitic

649   systems as silicalite (16.3 kJ mol^{-1}) and NaX (15.0 kJ mol^{-1}).[54]

650   From the comparison of the data reported in Table 3 it is evident that O_2 and N_2 have a

651   significantly lower affinity towards both the zeolite and the monolith with respect to CO_2.

652   Analogously to what previously discussed for CO_2, we denoted an increase in the affinity of both

653   N_2 and O_2 towards the monolith, because of the presence of Na^+ ions. The N_2 q_{st} calculated in

654   our study is very close to the average value obtained by Newsome and Coppens on a Na-ZSM-5

655   zeolite with slightly lower Si/Al ratio (23-25 kJ mol^{-1} with Si/Al ratio = 45)[58] or by Dunne et al.

656   (24.1 kJ mol^{-1} with Na-ZSM-5 with Si/Al ratio = 30)[54] indicating how the difference in Si/Al

657   ratio does not impact too much on the N_2 energetic of adsorption. It is interesting to notice that

658   whereas in the zeolite the q_{st} of N_2 and O_2 are quite identical, in the monolith the q_{st} of N_2 is

659   appreciably larger than for O_2 (24 vs. 15 kJ mol^{-1}). This is also evident from the isotherms

660   reported in Figure 7b and c, showing that whereas in the zeolite the N_2 and O_2 capacities are very

661   similar at all the pressures, in the monolith the N_2 adsorbed amount are always larger than the O_2

662   one in the same pressure and temperature conditions.

663

664 **Table 3**. Energetic of adsorption at the lower coverage for different adsorbates towards H-ZSM-5-800 and the

665 monolith.

Material	q_{st} CO_2 (kJ mol^{-1})	q_{st} O_2 (kJ mol^{-1})	q_{st} N_2 (kJ mol^{-1})	q_{st} H_2O (kJ mol^{-1})
H-ZSM-5-800	37 ± 4^{a}	14 ± 1^{a}	15 ± 1^{a}	120 ± 10^{b}
Monolith	49 ± 5^{a}	16 ± 2^{a}	24 ± 2^{a}	96 ± 9^{b}

666 ^{a}Isosteric heat, ^{b}microcalorimetry.
667

668 *IAST Selectivity.* The employment of any adsorbent material within post-combustion CO_2-

669 capture requires a high selectivity for CO_2 towards the other components of a post-combustion

670 gas stream; above all, the selectivity over N_2 is crucial, being this gas the most abundant in a

671 post-combustion mixture (75 vol.%). The selectivity of H-ZSM-5-800 and of the monolith for

672 CO_2/N_2 separation – in the presence of 5 vol.% O_2– were calculated by the use of IAST.[40, 41] The

673 power of IAST is to simulate multi-component isotherms at the desired composition (e.g. 15

674 vol.% CO_2, 80 vol.% N_2, 5 vol.% O_2) using, as initial guess, the single component isotherms

675 obtained experimentally (in our case reported in Figure 7a, 7b and 7c).

676 The IAST CO_2/N_2 selectivity in the presence of 5 vol.% O_2 has been calculated by means of

677 pyIAST software[41] for both H-ZSM-5-800 and the monolith, keeping the total pressure of 1 bar

678 constant and varying the CO_2 and N_2 partial pressures. Figure 10 reports the selectivity factors

679 for increasing CO_2 partial pressures.

680
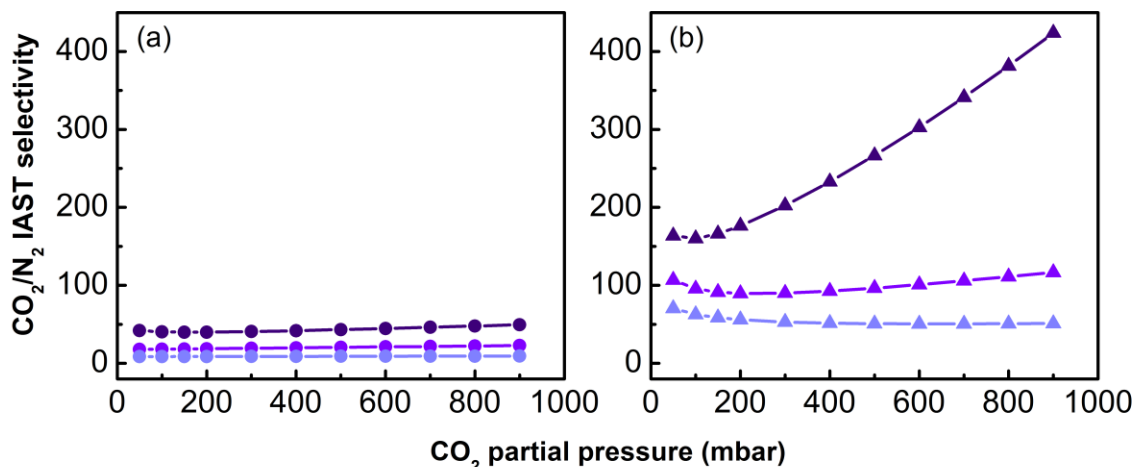
Figure 10   IAST CO_2/N_2 selectivity factors for a ternary $CO_2 : N_2 : O_2$ gas mixture (5 vol.% O_2 gas

mixture) at 1 bar and 25 (dark violet line), 60 (violet line) and 90 °C (light violet line) calculated from single

component isotherms reported in Figure 7a, 6b and 6c, for increasing CO_2 partial pressure. In the (a) part the data

calculated on the H-ZSM-5-800 are represented while on the (b) part the one on the monolith are reported.

Figure 10 is showing how the IAST CO_2/N_2 selectivity of the monolith is, at any temperature,

about three times than in the zeolite. These results suggest that also on this point of view, the

inclusion of the active phase in the final monolith has brought to a significant modification of its

CO_2-capture performances that is an improvement.

5. Conclusions

Several materials have been proposed for carbon capture but only few of them are conductive

and then suitable for their implementation in plants using ESA (electric swing adsorption).

Moreover, their incorporation as active phase in conductive carbons-based composites requires

them to bear the high temperatures involved during the manufacturing process (important for the

formation of the carbon phase); these temperatures are often out of the range of the thermal

697   stability of these adsorbents. In this work, the incorporation of H-ZSM-5 in a conductive

698   carbon/zeolite composite has been studied. The composite (78 wt.% of zeolite and 22 wt.% of

699   conductive carbon) has been obtained in a honeycomb monolith form, suitable for its final use in

700   a ESA CO_2-capture process. Besides a lower electric resistivity (5.8 Ω m versus 2500 Ω m),[61] the

701   monolith showed (i) improved CO_2 capacity, (ii) higher water working capacity; (iii) higher CO_2

702   interaction energy, (iv) higher specific heat capacity. In particular, XRD, TEM and N_2 volumetry

703   indicated that the zeolite structure was almost unaffected by the monolith preparation process.

704   TEM/EDS and IR spectroscopy suggested the possibility that one third of the protons was

705   exchanged by Na^+ ions during the pyrolysis step. A homogeneous grafting of the carbon phase

706   over the active phase was revealed by TEM images acquired at different magnifications.

707   CO_2 adsorption capacity of the honeycomb reference material was tested by means of volumetric

708   measurements till 1 bar and different temperatures (25, 60, 90 and 120°C). At room temperature

709   and 1 bar, the composite material is up-taking the same amount of CO_2 as the one registered for

710   the pure zeolite; conversely, a higher CO_2 uptake at 0.15 bar (+25 % of CO_2 adsorbed) is

711   observed for the monolith. Volumetric curves associated to the measurements performed at

712   higher temperatures always show higher profiles in case of honeycomb composite materials (1.5

713   vs 1.1 mol g^{-1} at 60 °C for the honeycomb monolith and for the H-ZSM-5-800 zeolite,

714   respectively). This can be related, besides to the higher defectivity of the monolith (and then

715   higher concentration of Si-OH and Al-OH species), to the higher affinity of CO_2 towards sodium

716   as counter-cation with respect of protons.

717   Although the monolith shows also a higher uptake of N_2 and O_2 with respect to H-ZSM-5-800,

718   the monolith IAST CO_2/N_2 selectivity (in the presence of 5 vol.% of O_2) is higher than for the

719   zeolite, at any temperature tested.

For what concerns water adsorption, a larger working capacity was predicted for the monolith than for the zeolite, due to the lower adsorption heat: this would suggest an easier removal of water contaminants (among the most energetics adsorbates in the flue gas) from the monolith, and then a less energy-demanding regeneration of the adsorbent in operative conditions.

As a final remark, this work underlined the properties gap between a pure active phase (the zeolite) and its related final artifact. This pointed out the importance of studying the adsorption properties of a sample designed to have shapes and physical-chemical characteristics as close as possible to the material that will be actually employed. This point is particularly important for engineer plant simulations, because the employment of parameters obtained on the active phase could bring to significant error in the process design.

ASSOCIATED CONTENT

Supporting Information. Pictorial representation of H-ZSM-5 structure, Particle distribution size from HRTEM, Thermogravimetric analysis of NH_4-ZSM-5 and the monolith, Specific heat capacity calculation, Adsorption isotherms at 25 °C of CO_2, N_2 and O_2, Calculation of the adsorption enthalpy of O_2 and N_2 on H-ZSM-5-800 by VTIR method, Data tables for CO_2, H_2O, N_2 and O_2 adsorption isotherms, Microcalorimetry of H_2O. This material is available free of charge via the Internet at http://pubs.acs.org.

AUTHOR INFORMATION

Corresponding Author

741   *Department of Chemistry, NIS Center and INSTM, University of Torino, via Quarello 15, I-

742   10135 Torino, Italy, Tel.: +390116708375, Fax: +390116707855; E-mail: jg.vitillo@gmail.com.

743   **Author Contributions**

744   The manuscript was written through contributions of all authors. All authors have given approval

745   to the final version of the manuscript.

755   ABBREVIATIONS

756   XRD, X-Ray Powder Diffraction; FTIR, Fourier-transformed infrared; MIR, medium infrared;

757   DSC, Differential Scan Calorimetry, CCS, Carbon Capture and Sequestration.

758   **REFERENCES**

759   1.   Thiruvenkatachari, R.; Su, S.; An, H.; Yu, X. X., Post combustion CO_2 capture by carbon
760   fibre monolithic adsorbents. *Prog. Energy Combust. Sci.* **2009,** 35, 438-455.
761   2.   Vitillo, J. G., Magnesium-based systems for carbon dioxide capture, storage and
762   recycling: from leaves to synthetic nanostructured materials. *RSC Adv.* **2015,** 5, 36192-36239.
763   3.   Sumida, K.; Rogow, D. L.; Mason, J. A.; McDonald, T. M.; Bloch, E. D.; Herm, Z. R.;
764   Bae, T. H.; Long, J. R., Carbon Dioxide Capture in Metal-Organic Frameworks. *Chem. Rev.*
765   **2012,** 112, 724-781.

766   4.   Samanta, A.; Zhao, A.; Shimizu, G. K. H.; Sarkar, P.; Gupta, R., Post-Combustion CO_2
767   Capture Using Solid Sorbents: A Review. *Ind. Eng. Chem. Res.* **2012,** 51, 1438-1463.
768   5.   Rochelle, G. T., Amine Scrubbing for CO_2 Capture. *Science* **2009,** 325, 1652-1654.
769   6.   DOE/NETL, Quality guidelines for energy system studies: CO_2 impurity design
770   parameters, Technical report. **2013**.
771   7.   Nikolaidis, G. N.; Kikkinides, E. S.; Georgiadis, M. C., Model-Based Approach for the
772   Evaluation of Materials and Processes for Post-Combustion Carbon Dioxide Capture from Flue
773   Gas by PSA/VSA Processes. *Ind. Eng. Chem. Res.* **2016,** 55, 635-646.
774   8.   Garcia, E. J.; Perez-Pellitero, J.; Jallut, C.; Pirngruber, G. D., Modeling Adsorption
775   Properties on the Basis of Microscopic, Molecular, and Structural Descriptors for Nonpolar
776   Adsorbents. *Langmuir* **2013,** 29, 9398-9409.
777   9.   Huck, J. M.; Lin, L. C.; Berger, A. H.; Shahrak, M. N.; Martin, R. L.; Bhown, A. S.;
778   Haranczyk, M.; Reuter, K.; Smit, B., Evaluating different classes of porous materials for carbon
779   capture. *Energy Environ. Sci.* **2014,** 7, 4132-4146.
780   10.   Fang, H. J.; Kulkarni, A.; Kamakoti, P.; Awati, R.; Ravikovitch, P. I.; Sholl, D. S.,
781   Identification of High-CO2-Capacity Cationic Zeolites by Accurate Computational Screening.
782   *Chem. Mat.* **2016,** 28, 3887-3896.
783   11.   Mason, J. A.; Sumida, K.; Herm, Z. R.; Krishna, R.; Long, J. R., Evaluating metal-
784   organic frameworks for post-combustion carbon dioxide capture via temperature swing
785   adsorption. *Energy Environ. Sci.* **2011,** 4, 3030-3040.
786   12.   Masala, A.; Vitillo, J. G.; Bonino, F.; Manzoli, M.; Grande, C. A.; Bordiga, S., New
787   insights into UTSA-16. *Phys. Chem. Chem. Phys.* **2016,** 18, 220-227.
788   13.   Das, A.; D'Alessandro, D. M., Tuning the Functional Sites in Metal-Organic Frameworks
789   to Modulate CO_2 Heats of Adsorption. *Crystengcomm* **2015,** 17, 706-718.
790   14.   Masala, A.; Grifasi, F.; Atzori, C.; Vitillo, J. G.; Mino, L.; Bonino, F.; Chierotti, M. R.;
791   Bordiga, S., CO_2 Adsorption Sites in UTSA-16: Multitechnique Approach. *J. Phys. Chem. C*
792   **2016,** 120, 12068-12074.
793   15.   Bolis, V., Fundamentals in Adsorption at the Solid-Gas Interface. Concepts and
794   Thermodynamics. In *Calorimetry and Thermal Methods in Catalysis*, Auroux, A., Ed. Springer
795   Berlin Heidelberg: Berlin, 2013; Vol. 154, pp 3-50.
796   16.   Khurana, M.; Farooq, S., Simulation and optimization of a 6-step dual-reflux VSA cycle
797   for post-combustion CO_2 capture. *Chem. Eng. Sci.* **2016,** 152, 507-515.
798   17.   Akhtar, F.; Keshavarzi, N.; Shakarova, D.; Cheung, O.; Hedin, N.; Bergstrom, L.,
799   Aluminophosphate monoliths with high CO_2-over-N_2 selectivity and CO_2 capture capacity. *RSC*
800   *Adv.* **2014,** 4, 55877-55883.
801   18.   Rezaei, F.; Webley, P., Structured adsorbents in gas separation processes. *Sep. Purif.*
802   *Technol.* **2010,** 70, 243-256.
803   19.   Rezaei, F.; Webley, P. A., Optimal design of engineered gas adsorbents: Pore-scale level.
804   *Chem. Eng. Sci.* **2012,** 69, 270-278.
805   20.   Menard, D.; Py, X.; Mazet, N., Activated carbon monolith of high thermal conductivity
806   for adsorption processes improvement Part A: Adsorption step. *Chem. Eng. Process.* **2005,** 44,
807   1029-1038.
808   21.   Grande, C. A.; Rodrigues, A. E., Electric Swing Adsorption for CO_2 removal from flue
809   gases. *Int. J. Greenh. Gas Control* **2008,** 2, 194-202.
810   22.   Ruthven, D. M., Past progress and future challenges in adsorption research. *Ind. Eng.*
811   *Chem. Res.* **2000,** 39, 2127-2131.

812   23.   Brandani, F.; Rouse, A.; Brandani, S.; Ruthven, D. M., Adsorption kinetics and dynamic
813   behavior of a carbon monolith. *Adsorpt.-J. Int. Adsorpt. Soc.* **2004,** 10, 99-109.
814   24.   Gorbach, A. B.; Stegmaier, M.; Eigenberger, G.; Hammer, J.; Fritz, H. G., Compact
815   pressure swing adsorption processes-impact and potential of new-type adsorbent-polymer
816   monoliths. *Adsorpt.-J. Int. Adsorpt. Soc.* **2005,** 11, 515-520.
817   25.   Grande, C. A.; Cavenati, S.; Barcia, P.; Hammer, J.; Fritz, H. G.; Rodrigues, A. E.,
818   Adsorption of propane and propylene in zeolite 4A honeycomb monolith. *Chem. Eng. Sci.* **2006,**
819   61, 3053-3067.
820   26.   Li, Y. Y.; Perera, S. P.; Crittenden, B. D., Zeolite monoliths for air separation part 2:
821   Oxygen enrichment, pressure drop and pressurization. *Chem. Eng. Res. Des.* **1998,** 76, 931-941.
822   27.   Gadkaree, K. P., Carbon honeycomb structures for adsorption applications. *Carbon* **1998,**
823   36, 981-989.
824   28.   Kreutzer, M. T.; Kapteijn, F.; Moulijn, J. A., Shouldn't catalysts shape up? Structured
825   reactors in general and gas-liquid monolith reactors in particular. *Catal. Today* **2006,** 111, 111-
826   118.
827   29.   Klett, J. W.; Burchell, T. D., Carbon fibre carbon composites for catalyst supports. . In
828   *Proceedings of the 22nd biennial conference on carbon*, Pergamon Press, University of
829   California: San Diego, CA, 1995.
830   30.   Thakkar, H.; Eastman, S.; Hajari, A.; Rownaghi, A. A.; Knox, J. C.; Rezaei, F., 3D-
831   Printed Zeolite Monoliths for CO2 Removal from Enclosed Environments. *ACS Appl. Mater.*
832   *Interfaces* **2016,** 8, 27753-27761.
833   31.   Couck, S.; Lefevere, J.; Mullens, S.; Protasova, L.; Meynen, V.; Desmet, G.; Baron, G.
834   V.; Denayer, J. F. M., CO2, CH4 and N-2 separation with a 3DFD-printed ZSM-5 monolith.
835   *Chem. Eng. J.* **2017,** 308, 719-726.
836   32.   Bagley, R., Method of forming an extrusion die. In Patent US3803951: 1974.
837   33.   Lachman, I. M.; Lewis, R. M., Anisotropic cordierite monolith. In US3885977 A: 1975.
838   34.   Andrzej Cybulski, J. A. M., *Structured Catalysts and Reactors*. CRC Press 2005; p 856.
839   35.   Farrauto, R. J.; Heck, R. M., Catalytic converters: state of the art and perspectives. *Catal.*
840   *Today* **1999,** 51, 351-360.
841   36.   Gregg, S. J.; Sing, K. S. W., *Adsorption surface area and porosity*. 2nd ed.; Academic
842   Press Inc.: London, 1982.
843   37.   Langmuir, I., The adsorption of gases on plane surfaces of glass, mica and platinum. *J.*
844   *Amer. Chem. Soc.* **1918,** 40, 1361-1403.
845   38.   Olivier, J. P., Modeling Physical Adsorption on Porous and Nonporous Solids Using
846   Density Functional Theory. *J. Porous Mat.* **1995,** 2, 9-17.
847   39.   Dalla Fontana, G.; Fiore, G. L.; Battezzati, L., Thermodynamics of the
848   Au49Ag5.5Pd2.3Cu26.9Si16.3 glass-forming alloy. *J. Non-Cryst. Solids* **2013,** 382, 95-98.
849   40.   Myers, A. L.; Prausnitz, J. M., Thermodynamics of mixed-gas adsorption. *AIChe Journal*
850   **1965,** 11, 121-127.
851   41.   Simon, C. M.; Smit, B.; Haranczyk, M., pyIAST: Ideal adsorbed solution theory (IAST)
852   Python package. *Computer Phys. Commun.* **2016,** 200, 364-380.
853   42.   Hoff, T. C.; Thilakaratne, R.; Gardner, D. W.; Brown, R. C.; Tessonnier, J. P., Thermal
854   Stability of Aluminum-Rich ZSM-5 Zeolites and Consequences on Aromatization Reactions. *J.*
855   *Phys. Chem. C* **2016,** 120, 20103-20113.
856   43.   Petrovic, I.; Navrotsky, A.; Davis, M. E.; Zones, S. I., Thermochemical Study of The
857   Stability of Frameworks in High-Silica Zeolites. *Chem. Mat.* **1993,** 5, 1805-1813.

858   44.   Ungár, T.; Gubicza, J.; Ribárik, G.; Pantea, C.; Zerda, T. W., Microstructure of carbon
859   blacks determined by X-ray diffraction profile analysis. *Carbon* **2002,** 40, 929-937.
860   45.   Vitillo, J. G.; Bordiga, S., Increasing the Stability of Mg_2(dobpdc) Metal-Organic
861   Framework in Air Through Solvent Removal. *Mater. Chem. Front.* **2017**, 10.1039/c6qm00220j.
862   46.   Thommes, M.; Kaneko, K.; Neimark, A. V.; Olivier, J. P.; Rodriguez-Reinoso, F.;
863   Rouquerol, J.; Sing, K. S. W., Physisorption of gases, with special reference to the evaluation of
864   surface area and pore size distribution (IUPAC Technical Report). *Pure Appl. Chem.* **2015,** 87,
865   1051-1069.
866   47.   Armandi, M.; Garrone, E.; Areán, C. O.; Bonelli, B., Thermodynamics of Carbon
867   Dioxide Adsorption on the Protonic Zeolite H-ZSM-5. *ChemPhysChem* **2009,** 10, 3316-3319 and
868   references therein.
869   48.   Pazé, C.; Bordiga, S.; Lamberti, C.; Salvalaggio, M.; Zecchina, A.; Bellussi, G., Acidic
870   Properties of H−β Zeolite As Probed by Bases with Proton Affinity in the 118−204 kcal mol^{-1}: A
871   FTIR Investigation. *J. Phys. Chem. B* **1997,** 101, 4740-4751.
872   49.   Weiland, R. H.; Dingman, J. C.; Cronin, D. B., Heat capacity of aqueous
873   monoethanolamine, diethanolamine, N-methyldiethanolamine, and N-methyldiethanolamine-
874   based blends with carbon dioxide. *J. Chem. Eng. Data* **1997,** 42, 1004-1006.
875   50.   Mu, B.; Walton, K. S., Thermal Analysis and Heat Capacity Study of Metal-Organic
876   Frameworks. *J. Phys. Chem. C* **2011,** 115, 22748-22754.
877   51.   Qiu, L. Y.; Laws, P. A.; Zhan, B. Z.; White, M. A., Thermodynamic investigations of
878   zeolites NaX and NaY. *Can. J. Chem.-Rev. Can. Chim.* **2006,** 84, 134-139.
879   52.   Qiu, L. Y.; Murashov, V.; White, M. A., Zeolite 4A: heat capacity and thermodynamic
880   properties. *Solid State Sci.* **2000,** 2, 841-846.
881   53.   Silva, G. G.; Musumeci, A. W.; Gomes, A. P.; Liu, J. W.; Waclawik, E. R.; George, G.
882   A.; Frost, R. L.; Pimenta, M. A., Characterization of commercial double-walled carbon nanotube
883   material: composition, structure, and heat capacity. *J. Mater. Sci.* **2009,** 44, 3498-3503.
884   54.   Dunne, J. A.; Rao, M.; Sircar, S.; Gorte, R. J.; Myers, A. L., Calorimetric heats of
885   adsorption and adsorption isotherms .2. O_2, N_2, Ar, CO_2, CH_4, C_2H_6, and SF_6 on NaX, H-ZSM-5,
886   and Na-ZSM-5 zeolites. *Langmuir* **1996,** 12, 5896-5904.
887   55.   Canivet, J.; Fateeva, A.; Guo, Y. M.; Coasne, B.; Farrusseng, D., Water adsorption in
888   MOFs: fundamentals and applications. *Chem. Soc. Rev.* **2014,** 43, 5594-5617.
889   56.   Ohlin, L.; Bazin, P.; Thibault-Starzyk, F.; Hedlund, J.; Grahn, M., Adsorption of CO_2,
890   CH_4, and H_2O in Zeolite ZSM-5 Studied Using In Situ ATR-FTIR Spectroscopy. *J. Phys. Chem.*
891   *C* **2013,** 117, 16972-16982.
892   57.   Masala, A.; Vitillo, J. V.; Mondino, G.; Grande, C. A.; Blom, R.; Manzoli, M.; Marshall,
893   M.; Bordiga, S., CO_2 capture in dry and wet conditions in UTSA-16 metal organic framework.
894   *ACS Appl. Mater. Interf.* **2016**.
895   58.   Newsome, D.; Gunawan, S.; Baron, G.; Denayer, J.; Coppens, M. O., Adsorption of CO_2
896   and N_2 in Na-ZSM-5: effects of Na+ and Al content studied by Grand Canonical Monte Carlo
897   simulations and experiments. *Adsorpt.-J. Int. Adsorpt. Soc.* **2013,** 20, 157-171.
898   59.   Arean, C. O.; Manoilova, O. V.; Palomino, G. T.; Delgado, M. R.; Tsyganenko, A. A.;
899   Bonelli, B.; Garrone, E., Variable-temperature infrared spectroscopy: An access to adsorption
900   thermodynamics of weakly interacting systems. *Phys. Chem. Chem. Phys.* **2002,** 4, 5713-5715.
901   60.   Delgado, M. R.; Area, C. O., Thermodynamics of nitrogen adsorption on the zeolite H-
902   FER. *Appl. Surf. Sci.* **2007,** 253, 5705-5708.

903   61.   Hussein, M. A.; Abu-Zied, B. M.; Asiri, A. M., Preparation, characterization, and
904   electrical properties of ZSM-5/PEG composite particles. *Polymer Comp.* **2014,** 35, 1160-1168.
905
906
907

908   Insert Table of Contents Graphic and Synopsis Here
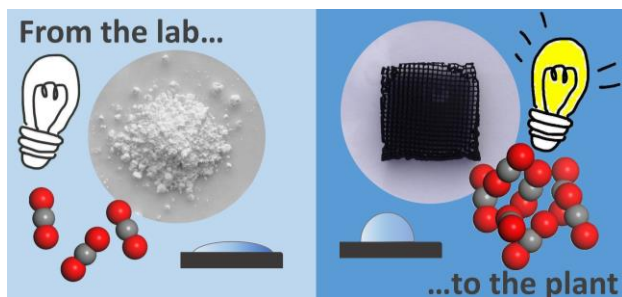
909

910   Carbon capture materials: from the lab to materials design. The inclusion of H-ZSM-5 in a

911   conductive carbon/zeolite monolith, suitable for Electric Swing Adsorption, showed decidedly

912   improved performances with respect to the pure zeolite in term of capacity and hydrophobility.

913